

MATERIALS SCIENCE

Discovery of multivalley Fermi surface responsible for the high thermoelectric performance in $\text{Yb}_{14}\text{MnSb}_{11}$ and $\text{Yb}_{14}\text{MgSb}_{11}$

Christopher J. Perez^{1*}, Maxwell Wood^{2*}, Francesco Ricci³, Guodong Yu^{3,4}, Trinh Vo⁵, Sabah K. Bux⁵, Geoffroy Hautier^{3†}, Gian-Marco Rignanese³, G. Jeffrey Snyder^{2‡}, Susan M. Kauzlarich^{1‡}

The Zintl phases, $\text{Yb}_{14}MSb_{11}$ ($M = \text{Mn, Mg, Al, Zn}$), are now some of the highest thermoelectric efficiency p-type materials with stability above 873 K. $\text{Yb}_{14}\text{MnSb}_{11}$ gained prominence as the first p-type thermoelectric material to double the efficiency of SiGe alloy, the heritage material in radioisotope thermoelectric generators used to power NASA's deep space exploration. This study investigates the solid solution of $\text{Yb}_{14}\text{Mg}_{1-x}\text{Al}_x\text{Sb}_{11}$ ($0 \leq x \leq 1$), which enables a full mapping of the metal-to-semiconductor transition. Using a combined theoretical and experimental approach, we show that a second, high valley degeneracy ($N_v = 8$) band is responsible for the groundbreaking performance of $\text{Yb}_{14}MSb_{11}$. This multiband understanding of the properties provides insight into other thermoelectric systems ($\text{La}_{3-x}\text{Te}_4$, SnTe , Ag_9AlSe_6 , and Eu_9CdSb_9), and the model predicts that an increase in carrier concentration can lead to $zT > 1.5$ in $\text{Yb}_{14}MSb_{11}$ systems.

INTRODUCTION

$\text{Yb}_{14}\text{MnSb}_{11}$ has received much attention since the thermoelectric properties were first reported because of a high thermoelectric figure of merit (zT) at high temperatures (800 to 1273 K) (1–4). After synthetic optimization, the zT has become ~300% larger than NASA's legacy p-type $\text{Si}_{1-x}\text{Ge}_x$ ($x \sim 0.5$) material used in radioisotope thermoelectric generators (RTGs) for space missions (2, 3, 5). With the recent increase in efficiency of $\text{Pr}_{3-x}\text{Te}_4$ (6), the high-temperature n-type material, improving the efficiency of this high-temperature p-type material further becomes an imperative for an overall efficient RTG. Recently, the thermoelectric properties of the isostructural $\text{Yb}_{14}\text{MgSb}_{11}$ have been shown to have a higher average zT from 800 to 1273 K without the detrimental increase to electrical resistivity from the spin-disorder arising from Mn (7). The efficiency of a thermoelectric generator depends, in part, on zT ($zT = \frac{S^2 T}{\rho \kappa}$), which is defined by the Seebeck coefficient (S), electrical resistivity (ρ), and thermal conductivity (κ). Improving the zT of $\text{Yb}_{14}\text{MSb}_{11}$ can reduce the cost of RTGs and allow larger payloads on future NASA missions. In addition, there is a need for thermoelectric generators that can recover waste heat in high-temperature applications such as aluminum smelting, cement kilns, and glass manufacturing (8). In this application, high-temperature thermoelectric generators made, in part, with $\text{Yb}_{14}\text{MSb}_{11}$ could recover up to 15% of waste heat (9). In this temperature range, only the half-Heusler compounds have comparable p-type performance (10). The complex

unit cell (Fig. 1) of $\text{Yb}_{14}\text{MnSb}_{11}$ can be described as consisting of Yb cations, MnSb_4 isolated tetrahedra, Sb_3 linear units, and isolated Sb anions, which lead to an ultralow thermal conductivity that plays a role in the realization of a large zT (3).

To date, $\text{Yb}_{14}MSb_{11}$ compounds have been understood as single-band semiconductors where the holes that provide the good thermoelectric performance have a relatively large effective mass, $m^* \sim 3 m_e$. Experimentalists often use a single parabolic band (SPB) model (effective mass model) (11) to predict and improve the thermoelectric transport properties of a material. Seebeck, electrical conductivity, and Hall effect data are used to calculate a material's effective mass m^* [Seebeck-derived density-of-states (DOS) mass], Hall mobility μ_H , and charge carrier concentration n_H as if the electron transport was coming from an SPB. SPB analysis has guided the optimized doping of half-Heuslers ($\text{Hf}_{0.65}\text{Zr}_{0.35}\text{Ni}_{1-x}\text{Pt}_x\text{Sn}_{0.98}\text{Sb}_{0.02}$), clathrates ($\text{Ba}_8\text{Ga}_{16}\text{Ge}_{30}$), and $\text{Mo}_3\text{Sb}_{7-x}\text{Te}_x$ (12–15). However, unexpected changes in the band structure and scattering with doping can lead to changes in the experimentally calculated m^* , which can point out deviations from SPB or simple phonon scattering.

Many well-known thermoelectric systems [$\text{Bi}_{2-x}\text{Sb}_x\text{Te}_3$ (16), $\text{Bi}_2\text{Te}_{3-x}\text{Se}_x$ (17), $\text{PbTe}_{1-x}\text{Se}_x$ (18), $\text{La}_{3-x}\text{Te}_4$ (19), CoSb_3 (20), and $\text{Mg}_2\text{Si}_{1-x}\text{Sn}_x$ (21)] have multiple electronic bands and have Fermi surfaces with high valley degeneracy and low band effective mass. This is because the maximum zT achievable by a thermoelectric material is generally determined by its quality factor $B \propto \frac{N_v}{m_b^* \kappa_L}$ where N_v is the valley degeneracy or number of Fermi surface pockets, m_b^* is the band effective mass of one valley, and κ_L is the lattice thermal conductivity (22). Materials with light band mass generally have high mobility, and high N_v leads to additional conducting pathways resulting in low electrical resistivity. An SPB analysis gives the DOS m^* that is larger than m_b^* by adding states from all N_v pockets contributing to electron transport, which is why good thermoelectric materials often have large DOS m^* . Multiband transport was frequently discovered in thermoelectric materials by noticing systematic changes in DOS m^* with alloying or doping.

SPB analysis has been used as a method for improving $A_{14}MPn_{14}$ (A = alkaline earth, Yb, Eu; M = Mn, Mg, Zn; Pn = group 15 element)

Copyright © 2021
The Authors, some
rights reserved;
exclusive licensee
American Association
for the Advancement
of Science. No claim to
original U.S. Government
Works. Distributed
under a Creative
Commons Attribution
NonCommercial
License 4.0 (CC BY-NC).

¹Department of Chemistry, University of California, Davis, One Shields Ave., Davis, CA 95616, USA. ²Department of Materials Science and Engineering, Northwestern University, Evanston, IL 60208, USA. ³Institute of Condensed Matter and Nanosciences, Université Catholique de Louvain, Louvain-la-Neuve 1348, Belgium. ⁴School of Physics and Technology, Wuhan University, Wuhan 430072, China. ⁵Thermal Energy Conversion Research and Advancement Group, Jet Propulsion Laboratory, California Institute of Technology, 4800 Oak Grove Drive, Pasadena, CA 91109-8099, USA.

*These authors contributed equally to this work.

†Present address: Thayer School of Engineering, Dartmouth College, Hanover, NH 03755, USA.

‡Corresponding author. Email: smkauzlarich@ucdavis.edu (S.M.K.); jeff.snyder@northwestern.edu (G.J.S.)

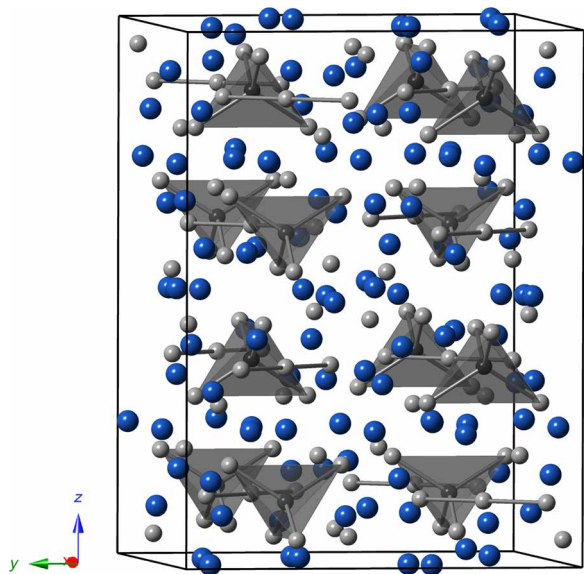


Fig. 1. A view of the unit cell of $A_{14}MSb_{11}$ ($A = Yb, Ca$; $M = Mg, Mn, Al$, or Zn). A atoms are indicated by blue spheres, MPn_4 are indicated by dark gray tetrahedra, Sb atoms are gray, and Sb_3 linear units are shown as bonded gray atoms.

materials with mixed results (4). In a study detailing the $Yb_{14}Mn_{1-x}Al_xSb_{11}$ solid solution, the slope of the samples' Seebeck coefficients changed as expected from a constant m^* as the carrier concentration was altered (23). However, this study could not explain why the Seebeck coefficient of differently doped samples appears to converge near room temperature instead of the expected 0 K for an SPB semiconductor with constant m^* (24). Hu *et al.* (4) and Kunz Wille *et al.* (25) have shown the experimental DOS effective mass of $A_{14}MPn_{11}$ markedly increases with increasing temperature and suggested a deviation from SPB.

Also anomalous, the thermal conductivity of $Yb_{14}MnSb_{11}$ (23), $Yb_{14}MgSb_{11}$ (26), $Sr_{14}MgSb_{11}$ (27), and $Eu_{14}MgSb_{11}$ (27) and other doped compositions of $Yb_{14}MnSb_{11}$ have an unexplained increase from ~ 300 to ~ 600 K. At 300 K, $Yb_{14}MnSb_{11}$ is above its Debye temperature (28), so the lattice thermal conductivity is expected to decrease proportionally as $1/T$ if Umklapp scattering dominates phonon transport, or temperature independent if diffusion (29) dominated. This would imply that the increase must come from the electronic portion of thermal conductivity; yet, an estimation of the electronic thermal conductivity results in a decreasing trend with increasing temperature (3, 26, 27, 30). A similar low temperature increase in thermal conductivity is also unexplained in $RE_{3-x}Te_4$ ($RE = Nd, La$) (31), $SnTe$ (32), Ag_9AlSe_6 (33), and Eu_9CdSb_9 (34). Using experimental and computational data, we build a three-band model, composed of two valence bands and one conduction band (CB), that attributes the anomalous transport behavior in $Yb_{14}Mg_{1-x}Al_xSb_{11}$ to a highly degenerate secondary band and shows the carrier concentration dependence on zT is opposite of what SPB predicts.

RESULTS AND DISCUSSION

DFT band structure

The computed band structures of $Yb_{14}MgSb_{11}$ and $Yb_{14}AlSb_{11}$ present similar features at the level of the valence bands involved in

transport (Fig. 2, A and B). In both compounds, the valence band maximum (VBM) is at Gamma (Γ), which is singly degenerate ($N_v = 1$). Both band diagrams display additional conducting states that are past the initial valence band at Γ with the energy offset (E_{offset}) between the VBM and the next valence band (VB_2) and that are very much alike in the two compounds ($E_{\text{offset},Mg} = 0.315$ eV and $E_{\text{offset},Al} = 0.295$ eV), which is stylized in Fig. 2C. The corresponding pocket of the Fermi surface (Fig. 2D) is at a low symmetry position between N-P, which gives it a high valley degeneracy, $N_v = 8$ (each pocket is on the Bragg planes of the Brillouin zone so that 16 half-pockets are shown). The calculated bandgap between the two compounds changes by a small amount from $E_{\text{gap},Mg} = 0.586$ eV to $E_{\text{gap},Al} = 0.463$ eV. The band structures also show that as Al is substituted by Mg, bands are filled, reducing the carrier concentration and moving the Fermi level up. For low x ($Yb_{14}Mg_{1-x}Al_xSb_{11}$), there will be holes deep into the valence band, indicating that samples with a larger carrier concentration or lower x will have more access to VB_2 . The orbital contribution can help experimentalists design future doping experiments and is shown in fig. S1 for $Yb_{14}MgSb_{11}$, $Yb_{14}MnSb_{11}$, $Ca_{14}MgSb_{11}$, and $Yb_{14}AlSb_{11}$. In all three compounds, the valence band is primarily composed of Yb -d and Sb -p states, while the CB is primarily composed of A (Yb, Ca) d states.

Synthesis of metal to insulator solution

Figure 3A shows the unit cell volume of $Yb_{14}Mg_{1-x}Al_xSb_{11}$ versus Al concentration. Overall, the volume of the unit cell systematically decreases as a function of increasing x . Compared with the structural changes in the solid solution of $Yb_{14}Mn_{1-x}Al_xSb_{11}$ where the angles of the MPn_4 became more idealized and the bond length became longer, the angles of the $Mg_{1-x}Al_xSb_4$ tetrahedron do not change significantly (fig. S2); instead, the $(Mg_{1-x}Al_x)_4Sb$ distance decreases as Mg is replaced with the smaller Al, leading to the contraction of the unit cell volume. Figure S2 also shows the a and c lattice parameters as a function of Al. As Al is substituted into the structure, a systematically increases and c decreases. The powder x-ray diffraction (PXRD) patterns and Rietveld refinement for $Yb_{14}Mg_{1-x}Al_xSb_{11}$ ($x = 0.0, 0.1, 0.3, 0.5, 0.7, 0.9, 1.0$) are provided (fig. S3 and table S1) and indicate good phase purity. Consistent with the unit cell volume, the nominal Al fraction and atomic percent values determined from electron microprobe analysis (EMPA) (fig. S4 and table S2) are within error of the nominal composition and have EMPA compositions within 3σ of the $Yb_{14}Mg_{1-x}Al_xSb_{11}$ formula unit.

Figure 3B shows carrier concentration and Hall mobility versus nominal Al fraction at 600 K. $Yb_{14}Mg_{1-x}Al_xSb_{11}$ initially increases and then systematically decreases with added Al as expected. At low x , the doping efficiency of Al is lower than expected. The lower than expected carrier concentration by about 63% could be due to the experimental uncertainty of the Hall measurement or indicate the presence of a compensating Yb valence or intrinsic defect manifestation. $Yb_{14}MgSb_{11}$ has been shown to contain Yb^{3+} and intermediate valent Yb by x-ray absorption near-edge structure (XANES), magnetic, and heat capacity studies (35, 36). $Yb_{14}ZnSb_{11}$, with the smallest unit cell reported to date and high carrier concentration, shows intermediate valent Yb (35, 36). In the case of $Yb_{14}Mg_{1-x}Al_xSb_{11}$, the smaller unit cell and disorder added with the solid solution may initially increase the tendency for intermediate valency until the carrier concentration is diminished (25, 36, 37). The addition of an extra electron from Al may be adjusting the amount of Yb^{3+} in the case of low x , buffering the system with intermediate valent Yb until

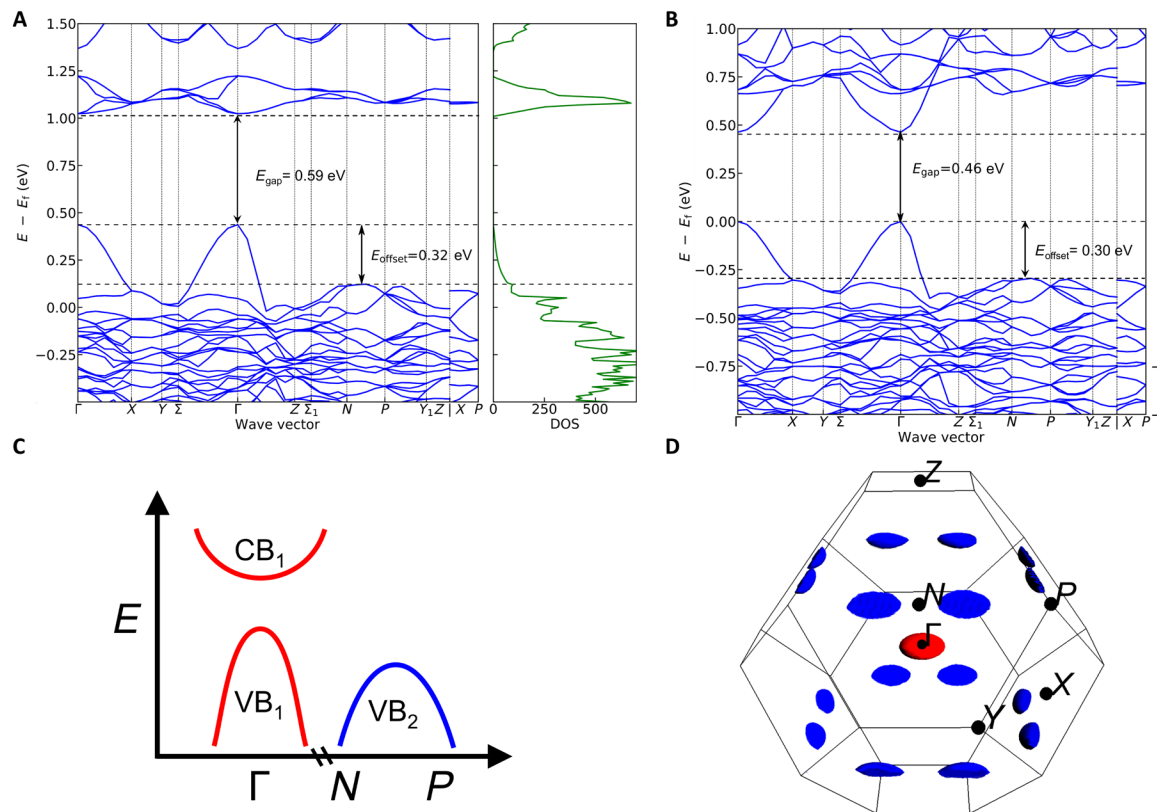


Fig. 2. A view of the band structures for Yb₁₄MSb₁₁ (M = Mg, Al) and the Fermi surfaces of the first two valence bands. (A) DFT band structure and density of states for Yb₁₄MgSb₁₁ where the Fermi level is at the top of the second valence band (VB₂). (B) DFT band structure for Yb₁₄AlSb₁₁ where the Fermi level is at the top of the first valence band (VB₁). (C) A schematic of the band structure used to understand electron transport for this solid solution, Yb₁₄Mg_{1-x}Al_xSb₁₁ containing both VB₁ and VB₂. (D) Fermi surface of VB₁ (red) centered at Γ and VB₂ (blue) between N and P containing 16 half-pockets. For comparisons to the band structure of Yb₁₄MnSb₁₁ and Ca₁₄MgSb₁₁, please see fig. S1.

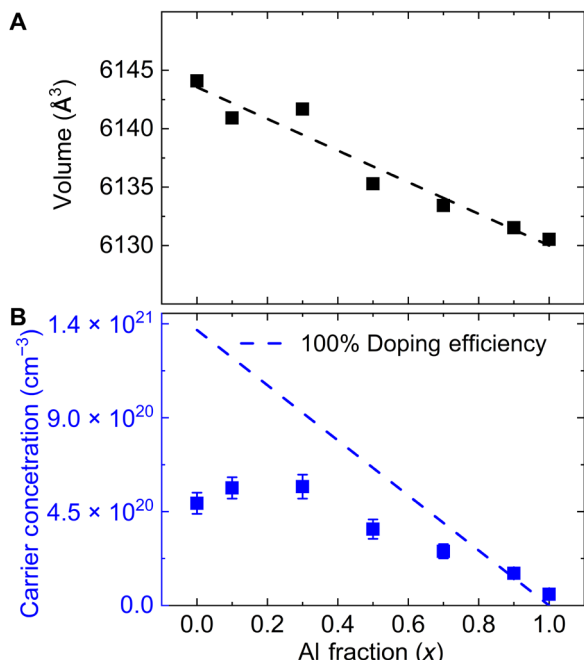


Fig. 3. Volume and carrier concentration of Yb₁₄Mg_{1-x}Al_xSb₁₁ as a function of x. (A) Nominal Al fraction (x) in Yb₁₄Mg_{1-x}Al_xSb₁₁ versus unit cell volume. As x increases, the unit cell volume decreases. (B) Carrier concentration versus nominal Al fraction, x, at 600 K for Yb₁₄Mg_{1-x}Al_xSb₁₁.

$x \sim 0.5$, thereby reflecting a lower than expected carrier concentration at low x . Intrinsic acceptor defects could also be playing a role at low Al concentrations, leading to the inconsistent trend.

Experiment and modeling of Seebeck, resistivity, and bandgap

The experimental Seebeck and resistivity temperature-dependent measurements are compared to the simulated Seebeck and resistivity in Fig. 4. A three-band model was used because the addition of a CB to the model describes the bipolar behavior that is witnessed in the experimental data. Experimentally, the Hall carrier concentrations of all compositions, x , are approximately constant until bipolar conduction appears at higher temperatures. To compare experimental data to the model, we plot different fixed carrier concentrations in the range of what is experimentally observed. Looking at the modeled output data, one can see the addition of a second valence band can cause the crossing of the Seebeck coefficient in $x = 0.1$ versus $x = 0.5$ ($n \sim 3 \times 10^{20}$ versus $n \sim 6 \times 10^{20}$ in Fig. 4) observed experimentally. This behavior, also seen in the Yb₁₄Mn_{1-x}Al_xSb₁₁ solid solution (23), cannot be explained from transport arising from an SPB and occurs due to the way the selection functions for electrical conductivity and Seebeck coefficient (VB₁ and VB₂; Fig. 2, B or C) sample differently the states from each band as a function of carrier concentration and temperature.

Another way of visualizing the impact the second valence band has on thermoelectric transport is through a Pisarenko plot (Fig. 5A),

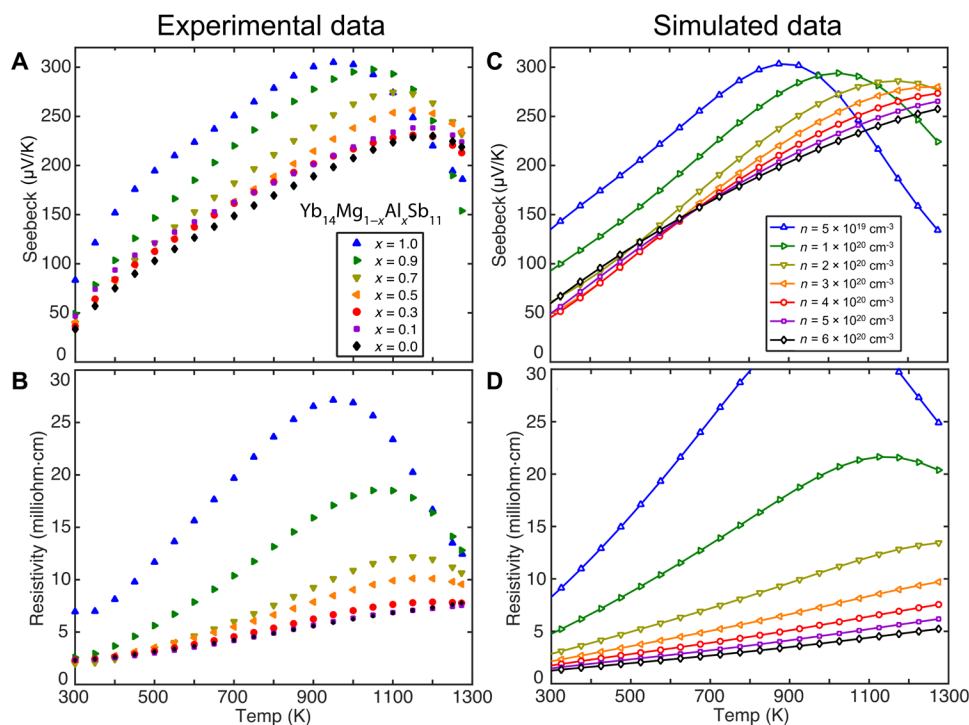


Fig. 4. Experimental and simulated Seebeck and resistivity data for $\text{Yb}_{14}\text{Mg}_{1-x}\text{Al}_x\text{Sb}_{11}$. Seebeck coefficient (A) and resistivity (B) versus temperature for experimental data $\text{Yb}_{14}\text{Mg}_{1-x}\text{Al}_x\text{Sb}_{11}$ ($x = 0.0, 0.1, 0.3, 0.5, 0.7, 0.9, 1.0$) compared with the simulated Seebeck coefficient (C) and resistivity (D) arising from the three-band model (see the Supplementary Materials for details). The simulation was generated with a fixed carrier concentration in the same range as what is experimentally observed. As Al fraction increases, the turnover in Seebeck coefficient and resistivity occurs at a lower temperature because of increased hole concentration. Note how the simulation shows the Seebeck coefficient of differently doped samples cross one another at ~ 600 K. This behavior that has previously been unexplained is witnessed in the experimental data as well as the previous solid solution study of $\text{Yb}_{14}\text{Mn}_{1-x}\text{Al}_x\text{Sb}_{11}$ (23). Note that the colors in the experimental data do not necessarily correspond exactly to the colors in the simulated data.

which shows the relationship between the carrier concentration and Seebeck coefficient of a material. At 400 K, the large increase in the DOS from the second valence band (VB_2) compared with only having the first valence band (VB_1) results in the increase in Seebeck coefficient that peaks around 10^{21} cm^{-3} carriers. At low temperatures and carrier concentrations, an SPB can well describe the transport properties of this solid solution. However, at higher temperatures, the Fermi-Dirac distribution is broader and samples this higher DOS band, resulting in Seebeck coefficients larger than what an SPB model would predict as seen in Fig. 5 (A and B). In addition, at higher carrier concentrations, the Fermi level of the material is pushed down closer to the band edge of VB_2 (Fig. 2B), thereby making the Fermi-Dirac distribution more likely to select those states. Analyzing the transport arising from these two bands as if it were coming from a single band, done in an effective mass analysis, would result in the resulting DOS effective mass increasing with increasing temperature and carrier concentration (fig. S5). This increase in effective mass with temperature and carrier concentration is what previous experimental studies (4, 25) have been reported for different compounds of the $A_{14}MPn_{11}$ structure and is seen in Fig. 5B. A typical SPB model would predict Seebeck decreases as a function of carrier concentration, but as seen in Fig. 5B, our multiple-band model predicts the observed retention or increase in Seebeck with increasing carrier concentration. As a result, the Seebeck can be increased without increasing electrical resistivity, leading to the maximum power factors ($\text{PF} = \frac{S^2}{\rho}$) at $x = 0.1$ and 0.3 (Fig. 5C).

As the composition of the solid solution is varied from the $\text{Yb}_{14}\text{MgSb}_{11}$ end member to $\text{Yb}_{14}\text{AlSb}_{11}$, the carrier concentration decreases, and the Fermi level is moved closer to the CB. This can explain why $\text{Yb}_{14}\text{AlSb}_{11}$ experiences a maximum in Seebeck and resistivity at a lower temperature than other samples and then is followed in successive order by samples with increasing Mg content. At elevated temperatures, where the Fermi-Dirac distribution is very broad, the least doped material will be the first to have states from the CB (Fig. 2C) sampled, thereby activating minority carriers. The experimental bandgap calculated from the Goldsmid and Sharp expression ($E_g = 2eS_{\text{max}}T_{\text{max}}$) (fig. S6) does not significantly change as a function of composition and is very close to the computed density functional theory (DFT) value for $\text{Yb}_{14}\text{MgSb}_{11}$ ($E_{\text{gap}} = 0.586$ eV), which supports that the change in the onset of bipolar conduction is due to doping (38).

Impact of the multiband electronic structure on the thermal conductivity

The temperature dependence of thermal conductivity (Fig. 6A) of the highly doped samples is rather unusual, although similar behavior has been reported in other $A_{14}MPn_{11}$ materials (3, 26). At intermediate temperatures (600 to 900 K), the reduction in thermal conductivity with increasing temperature can be explained via additional phonon scattering. The high-temperature behavior (≥ 900 K) increase with increasing temperature can be explained with bipolar conduction, while the low temperature increase (300 to 600 K) in thermal conductivity has been previously misattributed to lattice thermal

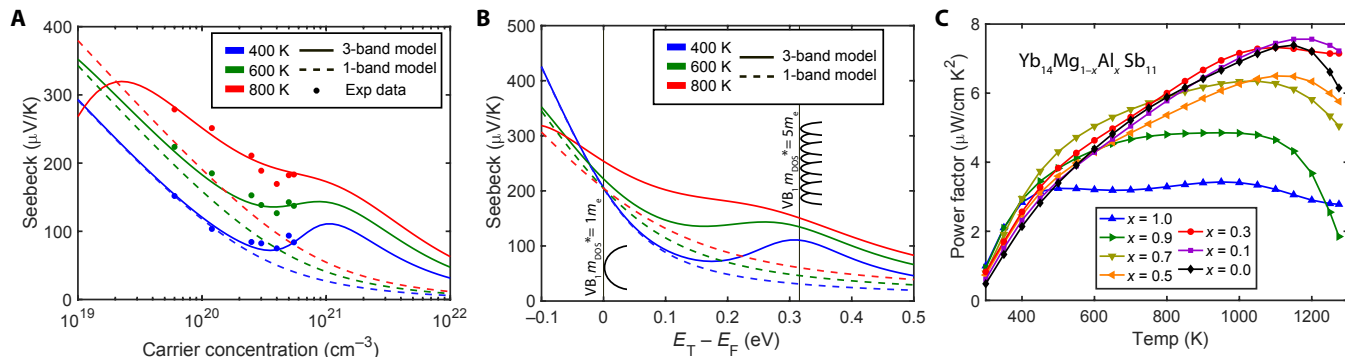


Fig. 5. Comparison of SPB with the 3-band model. (A) Pisarenko plot for samples made in this study. Points are measured values 400 K (blue), 600 K (green), and 800 K (red). The dashed lines give the relationship between Seebeck coefficient and carrier concentration for a material with a single parabolic band with an effective mass of $1m_e$ at these temperatures. The solid lines give the relationship between Seebeck coefficient and carrier concentration for a material with two valence bands offset in energy by 0.315 eV with the same intrinsic mobility but different masses ($VB_1, m^* = 1m_e$; $VB_2, m^* = 5m_e$) and (B) Seebeck coefficient versus Fermi level relative to the band edge of the VB_1 at 400 K (blue), 600 K (green), and 800 K (red) for a single parabolic band (dashed lines) and the three-band (solid lines) model described here. Notice the local maximum in Seebeck that results close to the band edge of the second valence band (VB_2). (C) Power factor versus temperature for $Yb_{14}Mg_{1-x}Al_xSb_{11}$ ($x = 0.0, 0.1, 0.3, 0.5, 0.7, 0.9, 1.0$).

conductivity (23). We can now attribute the low temperature increase to electronic effect arising from the second valence band (VB_2 ; Fig. 2C). This is qualitatively seen in the simulated electronic thermal conductivity (Fig. 6B), which as carriers are excited from the first valence band to the second valence band with increasing temperature there is a bipolar-like effect that occurs (Model Inputs and Visualization in Supplementary Materials). Unfortunately, the overall magnitude of the simulated electronic thermal conductivity is overestimated. This overestimation may have been the result of our model not considering intervalley scattering, which can have an effect on lowering a material's Lorenz number (39–41). Therefore, while an accurate lattice thermal conductivity of this material cannot be calculated, we can qualitatively explain the temperature dependence of the thermal conductivity. This multiband model could also be used to explain the unexplained increase in thermal conductivity at low temperatures seen in $RE_{3-x}Te_4$ ($RE = Nd, La$) (31), SnTe (32), Ag_9AlSe_6 (33), and Eu_9CdSb_9 (34). These phases have reported electronic structures, and while the effect the multiband nature of the electronic structures has on transport properties is acknowledged, an explanation for their low-temperature thermal conductivity is not discussed and is most likely also affected by multiple bands. Understanding the impact of the multiband nature on the low-temperature thermal conductivity ultimately helps in designing better thermoelectric materials.

Power factor and zT

Samples' zT s versus carrier concentrations are plotted in Fig. 7A compared with the three-band model described here and a model that uses only an SPB. The SPB model was created using only the model parameters for the first valence band at Γ (VB_1) and describes the low-temperature behavior well. To create a more accurate estimation of zT versus carrier concentration, we used the three-band electronic transport simulation described here and a fixed lattice thermal conductivity of 0.3 W/mK. This estimation is reasonable given the complexity of the material's crystal structure that likely leads the lattice thermal conductivity to be diffusion dominated (29). We should note that while our model does not account for intervalley scattering, there is a rough canceling of errors as the significantly overestimated electronic thermal conductivity that is part of the denominator of zT is offset by the slightly overestimated

Seebeck coefficient and conductivity that forms the numerator. On the basis of Fig. 7, one can surmise the second heavier valence band (VB_2) has significantly better thermoelectric transport than the first band (VB_1). While larger single-band effective masses in materials are generally considered detrimental to a material's zT (42), the high degeneracy ($N_v = 8$) of the second valence band has the effect of splitting its states into multiple conducting pathways. This has the effect of reducing electron-phonon scattering that would normally be expected from a high-DOS band (43). Modeling the transport arising from only these three bands suggests even higher zT s may be possible for $Yb_{14}MSb_{11}$ ($M = Mn, Mg, Al, Zn$) if a suitable dopant is found that can increase the carrier concentration of the material such as alkali metals or another +1 metal replacing Yb or Sn/Ge replacing Sb (44, 45). This is contrary to the conclusion reached using an SPB model to analyze the $Yb_{14}Mn_{1-x}Al_xSb_{11}$ solid solution, in which the lower carrier concentration $Yb_{14}Mn_{0.2}Al_{0.8}Sb_{11}$ had the highest zT (23). In this case, an increase in spin disorder scattering from replacing Al with Mn likely obscured the benefits the second valence band had at higher carrier concentrations (46). In $Yb_{14}Mg_{1-x}Al_xSb_{11}$ series of samples, the $x = 0.1$ and 0.3 samples that have the highest carrier concentration and power factor also have the highest zT (Fig. 7B).

$Yb_{14}Mg_{1-x}Al_xSb_{11}$ ($x = 0.0, 0.1, 0.3, 0.5, 0.7, 0.9, 1.0$) was synthesized by high-energy mechanical milling and high-temperature annealing. Using DFT-guided semiempirical modeling, we show that a highly degenerate ($N_v = 8$) second valence band is responsible for the good electronic thermoelectric properties of $Yb_{14}Mg_{1-x}Al_xSb_{11}$. By considering the effects of this second band, we can explain the peculiar temperature dependency of thermal conductivity and carrier concentration dependence of Seebeck coefficient of the materials in this solid solution and can potentially apply our second band analysis to other promising thermoelectric materials. Using the multiband model, we create a more accurate prediction of the carrier concentration dependence of zT , which shows that increasing the carrier concentration of $Yb_{14}MSb_{11}$ ($M = Mn, Mg, Al, Zn$) could result in even better thermoelectric performance. Assuming the band structure of the $A_{14}MPn_{11}$ structure type holds across different compositions, this work opens a new strategy for optimization for zT improvements and could lead to groundbreaking thermoelectric performance.

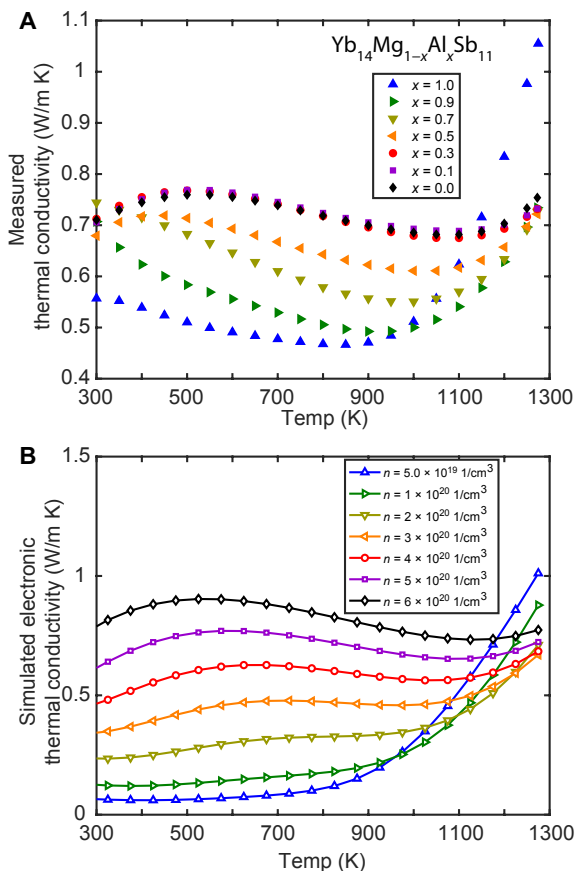


Fig. 6. Experimental and simulated thermal conductivity. (A) Experimental thermal conductivity (κ_{tot}) versus temperature for $\text{Yb}_{14}\text{Mg}_{1-x}\text{Al}_x\text{Sb}_{11}$ ($x = 0, 0.1, 0.3, 0.5, 0.7, 0.9, 1.0$), compared with (B) simulated electronic thermal conductivity. Note that at high doping levels, the simulated electronic thermal conductivity displays the same increase versus temperature that the experimental data experiences. This behavior has previously been attributed to the material's lattice thermal conductivity but can be rationalized as a bipolar-like effect between the two valence bands. Now, our model likely overestimates the magnitude of electronic thermal conductivity because intervalley scattering processes are not taken into effect. Note the colors in the experimental data do not necessarily correspond exactly to the colors in the simulated data.

METHODS

Materials

Materials were manipulated in an argon-filled glove box under 1 part per million of water. Mg turnings (99+, Strem Chemicals), Sb shot (99.999%, 5N Plus), and fresh Yb filings (<2 mm) were prepared using a large-toothed steel rasp from a Yb ingot (99.95%, Edge Tech) cleaned with a wire brush before use, and Al filings (<2 mm) were prepared from Al shot (99.999%, Alfa Aesar) using a large-toothed steel rasp after arc-welding under argon to remove oxide and cleaned with a steel brush.

Synthesis of Mg_3Sb_2

Synthesis was adapted from the literature (30). Ten grams of stoichiometric Mg and Sb was placed in a SPEX tungsten carbide grinding vial set (55 ml, 2 ¼ inches diameter by 2 ½ inches length) with three ~10.75-g tungsten carbide balls. The vial was hermetically sealed with custom Viton O-rings and mechanically milled for an hour using a SPEX 8000D mixer/miller. Clumpy black powder (5 g) was removed using a chisel and placed in a 10-cm Ta tube that was

sealed under Ar. The Ta tube was jacketed in a fused silica tube under vacuum and annealed at 800°C for 7 days. The result was a solid black ingot that was smashed out of the container using a hammer. The sample was confirmed phase pure by PXRD as shown in the Supplementary Materials (fig. S7).

Synthesis of $\text{Yb}_{14}\text{Mg}_{1-x}\text{Al}_x\text{Sb}_{11}$

Synthesis was adapted from the literature (3, 30). First, it was experimentally determined that the $\text{Yb}_{14}\text{MgSb}_{11}$ end member required 14.02Yb:1.2Mg:Sb11 to obtain a phase pure product. Next, it was determined that $\text{Yb}_{14}\text{AlSb}_{11}$ required 14.02Yb:1.05Al:Sb11 to obtain a phase pure product. A linear fit ($y = -0.15x + 0.2$), where $x = \text{Al}$ fraction and $y = \text{Mg/Al}$ excess, was used to determine the excess Al/Mg at a given Al fraction (x) according to the formula $\text{Yb}_{14}\text{Mg}_{1-x}\text{Al}_x\text{Sb}_{11}$, where 80% of the excess was Mg and 20% of the excess was Al. $\text{Yb}_{14}\text{Mg}_{1-x}\text{Al}_x\text{Sb}_{11}$ was synthesized by placing $\frac{(1-x)+(y \times 0.8)}{3} \text{Mg}_3\text{Sb}_2$, $11 - \left(2 \times \frac{(1-x)+(y \times 0.8)}{3}\right) \text{Sb}$, and $(x + (y \times 0.2))\text{Al}$ in the hermetically sealed tungsten carbide milling setup described above with two ~10.75-g tungsten carbide balls and mechanically milled for 15 min, producing a fine black powder. In addition, 14.02Yb was added to the mixture and milled for 30 min, resulting in black powder with some small chunks, which was scraped out of the tungsten carbide vial with a chisel. The powder (5 g) was placed in a 7.5-cm Nb tube and then arc-welded shut under an Ar atmosphere. The Nb tube was jacketed with a fused silica tube under vacuum and then placed in an alumina cup to ensure even heating. The samples were heated in a box furnace to 850°C at a rate of 50°C/hour and held at 850°C for 96 hours and then let cool to room temperature. The reaction vessels were opened inside a glove box. The result was a fine black powder with some annealed chunks. A 100-mesh sieve was used to exclude any large pieces, yielding ~4 g of powder. The sample was then prepared for spark plasma sintering (SPS) and PXRD.

Powder x-ray diffraction

Diffraction experiments were performed using a Bruker D8 Eco Advance diffractometer operated at 40 kV and 25 mA at 298 K using $\text{Cu K}\alpha$ radiation ($\lambda = 1.5405 \text{ \AA}$). Data were collected from 15° to 90° 2θ at a 0.0194° step size. Si powder (~2 weight %; Fisher Scientific, 99.999%) was ground into the sample to provide a calibration standard for lattice parameters. JANA 2006 software package was used for Rietveld refinement (47). Models for Rietveld refinement were generated from Si and $\text{Yb}_{14}\text{MgSb}_{11}$ crystallographic information files (26, 48). Sample height correction, manual background, and lattice parameters were fit first. A pseudo-Voigt function was used to generate the profile shape. Estimated standard deviations (ESDs) were multiplied by Berar's factor to give realistic values (49). Mg-Al fraction was not refined because of similarity in Mg/Al x-ray scattering factors.

Spark plasma sintering

Powder (~3 g) was loaded into a 12.7-mm-diameter graphite die with graphite plungers and 12 sheets of graphite foil on each side to ensure air-free conditions and avoid having the sample stick to the plungers. The die was inserted into a Dr. Sinter-Lab Jr. SPS-2ll LX with a thermocouple inserted into a hole drilled in the side of the die. The material was initially cold pressed at 28 MPa (on the cross section). During sintering, the sample was pressurized to 15 MPa (on the cross section) for 4 min, and then, the pressure was increased to 55 MPa (on the cross section) over 2 min and held for the remaining 15 min. The sample was simultaneously heated from

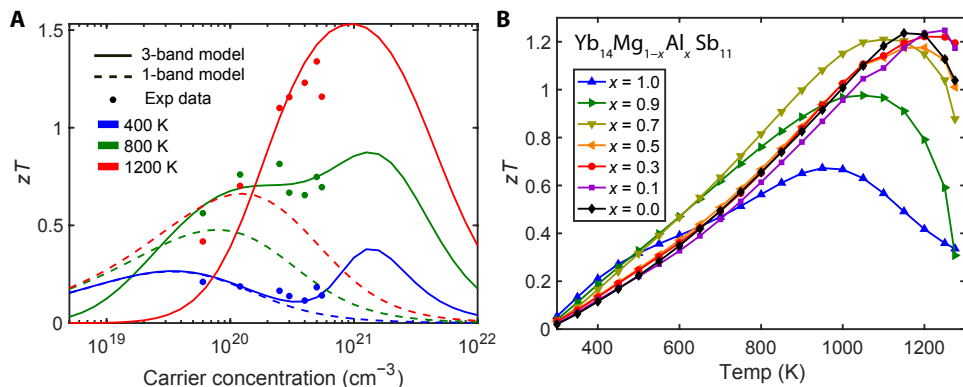


Fig. 7. Carrier concentration dependence of zT . (A) zT versus carrier concentration for $\text{Yb}_{14}\text{Mg}_{1-x}\text{Al}_x\text{Sb}_{11}$ ($x = 0.0, 0.1, 0.3, 0.5, 0.7, 0.9, 1.0$) compared with a single parabolic band model and the three-band model described here. While a single parabolic band model can describe low-temperature data reasonably well, it completely fails at predicting the temperature-dependent data and at instructing experimentalists the ideal carrier concentration to dope their materials. The work done here suggests that increasing the carrier concentration of $\text{Yb}_{14}\text{MgSb}_{11}$ could lead to even further enhancement in the material's zT . (B) Temperature-dependent zT . The samples with the highest carrier concentration ($x = 0.1$ and 0.3) have the highest zT .

room temperature to 750°C over 5 min and then to 800°C over 1 min and held at 800°C for 15 min. The result was a ~3-mm-thick black/metallic puck that was cut into ~1-mm-thick disks for laser flash analysis (LFA), Hall effect, and Seebeck coefficient measurements. Sample density was geometrically determined. All samples were >97% of crystallographic density.

Electron microprobe analysis

Electron microprobe measurements were on sintered pellets mounted in epoxy and polished to a 1-μm finish. A Cameca SX100 Electron Probe Microanalyzer with five wavelength-dispersive spectrometers was used. A single crystal of $\text{Yb}_{14}\text{MgSb}_{11}$ was used for the $\text{Yb L}\alpha 1$, $\text{Mg K}\alpha 1$, and $\text{Sb L}\alpha 1$ standard. The $\text{K}\alpha 1$ of Al was standardized from an alumina standard. Compositions were calculated by averaging 10 data points and multiplying by 0.26 (the number of atoms in one formula unit of $\text{Yb}_{14}\text{MgSb}_{11}$).

Thermal conductivity

Thermal diffusivity was measured on ~1-mm-thick sintered pellets polished flat and parallel and sprayed with graphite to ensure laser absorption. A Netzsch LFA 457 laser flash system was used. Diffusivity data are shown in fig. S8. Thermal conductivity was calculated using $\kappa = D \times C_p \times \delta$, where D is the measured diffusivity and δ is the temperature-adjusted density for $\text{Yb}_{14}\text{MnSb}_{11}$ (50). C_p measurements on $\text{Yb}_{14}\text{Mn}_{1-x}\text{Al}_x\text{Sb}_{11}$ single crystals grown from tin flux showed that the C_p was constant for samples of the composition $x = 0.2$ to $x = 0.95$, indicating that the M site in the $\text{Yb}_{14}\text{MSb}_{11}$ structure has minimal contribution to the heat capacity of $\text{Yb}_{14}\text{MnSb}_{11}$ (51), so the C_p reported on sintered pellets of $\text{Yb}_{14}\text{MnSb}_{11}$ will be used (3).

Hall effect and resistivity measurements

Temperature-dependent Hall effect and resistivity measurements were performed on flat and parallel sintered pellets using a custom instrument that uses the van der Pauw method with tungsten contacts and a 0.8-T magnet under high vacuum (52). A heating rate of 180 K/hour was used. For viewing ease and zT calculations, data were fit with a sixth-order polynomial. Experimental data are shown in fig. S8.

Seebeck coefficient measurements

The Seebeck coefficient was measured on sintered pellets using a custom-built instrument using the light pulse method. Tungsten-niobium thermocouples were used (53). For viewing ease and zT calculations, data were fit with a sixth-order polynomial. Experimental data are shown in fig. S8. As Al increases, samples have a hysteresis in Seebeck and resistivity data, but not thermal conductivity data. When samples are polished and remeasured, the data are reproduced (fig. S9). Scanning electron microscopy (SEM)/energy-dispersive X-ray spectroscopy (EDS) analysis after cycling shows the surface of the samples that are coated with Yb_2O_3 (fig. S9), which impede electrical contact with measurement probes, but after polishing, the samples are intact.

Density functional theory

The electronic band structures were calculated within DFT, using the Vienna Ab initio Simulation Package (VASP) (54, 55) with the Perdew-Burke-Ernzerhof (PBE) generalized gradient approximation (GGA) functional and adopting the projector augmented-wave (PAW) (56, 57) approach. The Yb pseudopotential has the 4f electrons frozen in the core (i.e., not as valence electrons). This was motivated by a previous x-ray photoelectron spectroscopy (XPS) study, which indicated that Yb-4f states in $\text{Yb}_{14}\text{MnSb}_{11}$ and $\text{Yb}_{14}\text{ZnSb}_{11}$ are below the Fermi level by more than 0.5 and 1 eV, respectively (37). We also performed some tests with the PAW Yb pseudopotential providing f electrons as valence electrons and applying different Hubbard U values on the f states. The typical U values used in previous work on other Yb antimonides (58) lead to f states much lower than the valence bands, confirming that f states could be neglected shown in fig. S10. The primitive structures were relaxed until the forces are less than 0.01 eV/Å. During the relaxations and static runs, the wave functions were expanded on a plane-wave basis setup to an energy cutoff of 520 eV, and the Brillouin zone was sampled using a $2 \times 2 \times 2$ Monkhorst-Pack k -point grid. A non-self-consistent field calculation on an $8 \times 8 \times 8$ k -point grid was performed to calculate the DOS and the Fermi surface. Then, by using the BoltzTraP (59, 60) software, the eigenvalues were interpolated on a 10 times denser grid to obtain the DOS, and on a 100 times denser grid to obtain the Fermi surface. Pymatgen (61, 62) was used for postprocessing,

such as plotting the band structure on the standard high-symmetry k -point path (63) and the Fermi surface.

Multiparabolic band model

For the modeled transport data, a three-band model was created using DFT inputs from $\text{Yb}_{14}\text{MgSb}_{11}$ for the band offsets between the two CBs ($E_{\text{offset}} = 0.315$ eV) and the bandgap ($E_{\text{gap}} = 0.586$ eV). Additional inputs needed for this model are the intrinsic mobility and effective mass of each band. We find that the following parameters qualitatively describe the experimental data measured; however, slight adjustments in these parameters would also likely suffice. The intrinsic mobility for each band was set at $25 \text{ cm}^2/\text{Vs}$ at 300 K and decreased proportionally to $T^{-1.5}$ with temperature. The DOS mass of the first valence band (m^*_{Vb1}) was set to $1m_e$, the DOS mass of the second valence band (m^*_{Vb2}) was set to $5m_e$, and the DOS mass of the CB (m^*_{CB}) was set to $4m_e$. For all simulated data, the carrier concentration was kept fixed and the Fermi level was varied with temperature to ensure charge neutrality of the simulated sample (11, 24). We would like to point out that the features in the Seebeck coefficient and thermal conductivity versus temperature and doping level that this paper set out to investigate cannot be explained by a transport function of a single band and require the two valence bands offset in energy to be accurately described.

Supporting information

Supporting Information is available: band structures for $\text{Yb}_{14}\text{MgSb}_{11}$, $\text{Ca}_{14}\text{MgSb}_{11}$, $\text{Yb}_{14}\text{AlSb}_{11}$, and $\text{Yb}_{14}\text{MnSb}_{11}$; lattice parameters and M-Sb distances for $\text{Yb}_{14}\text{Mg}_{1-x}\text{Al}_x\text{Sb}_{11}$; Rietveld refinement plots and resulting parameters; plot of Al content from EMPA versus x ; electron microprobe analysis; carrier concentration and Hall mobility plots; bandgap calculated from Goldsmid and Sharp expression; PXRD data for Mg_3Sb_2 ; Seebeck and resistivity data; SEM/EDS of $\text{Yb}_{14}\text{AlSb}_{11}$; cycled Seebeck data for $\text{Yb}_{14}\text{Mg}_{0.5}\text{Al}_{0.5}\text{Sb}_{11}$; band structures of $\text{Yb}_{14}\text{AlSb}_{11}$ with Hubbard U ; model inputs and visualization; transport functions; effective mass model; additional bands; and temperature considerations.

SUPPLEMENTARY MATERIALS

Supplementary material for this article is available at <http://advances.sciencemag.org/cgi/content/full/7/4/eabe9439/DC1>

REFERENCES AND NOTES

1. G. J. Snyder, E. S. Toberer, Complex thermoelectric materials. *Nat. Mater.* **7**, 105–114 (2008).
2. S. R. Brown, S. M. Kauzlarich, F. Gascoin, G. J. Snyder, $\text{Yb}_{14}\text{MnSb}_{11}$: New high efficiency thermoelectric material for power generation. *Chem. Mater.* **18**, 1873–1877 (2006).
3. J. H. Grebenkemper, Y. Hu, D. Barrett, P. Gogna, C.-K. Huang, S. K. Bux, S. M. Kauzlarich, High temperature thermoelectric properties of $\text{Yb}_{14}\text{MnSb}_{11}$ prepared from reaction of MnSb with the elements. *Chem. Mater.* **27**, 5791–5798 (2015).
4. Y. Hu, G. Cerretti, E. L. K. Wille, S. K. Bux, S. M. Kauzlarich, The remarkable crystal chemistry of the $\text{Ca}_{14}\text{AlSb}_{11}$ structure type, magnetic and thermoelectric properties. *J. Solid State Chem.* **271**, 88–102 (2019).
5. J.-P. Fleurial, Thermoelectric power generation materials: Technology and application opportunities. *JOM* **61**, 79–85 (2009).
6. D. Cheikh, B. E. Hogan, T. Vo, P. Von Allmen, K. Lee, D. M. Smiadak, A. Zevalkink, B. S. Dunn, J.-P. Fleurial, S. K. Bux, Praseodymium telluride: A high-temperature, high-ZT thermoelectric material. *Joule* **2**, 698–709 (2018).
7. A. P. Justl, G. Cerretti, S. K. Bux, S. Kauzlarich, Hydride assisted synthesis of the high temperature thermoelectric phase: $\text{Yb}_{14}\text{MgSb}_{11}$. *J. Appl. Phys.* **126**, 165106 (2019).
8. T. Hendricks, W. T. Choate, *Engineering Scoping Study of Thermoelectric Generator Systems for Industrial Waste Heat Recovery* (U.S. Department of Energy, 2006).
9. J.-P. Fleurial, S. Bux, T. Caillat, *Engineering of Novel Thermoelectric Materials and Devices for Next Generation, Long Life, 20% Efficient Space Power Systems*, in *11th International Energy Conversion Engineering Conference (Thermoelectric Devices and Systems*, 2013).
10. H. Zhu, J. Mao, Y. Li, J. Sun, Y. Wang, Q. Zhu, G. Li, Q. Song, J. Zhou, Y. Fu, R. He, T. Tong, Z. Liu, W. Ren, L. You, Z. Wang, J. Luo, A. Sotnikov, J. Bao, K. Nielsch, G. Chen, D. J. Singh, Z. Ren, Discovery of TaFeSb -based half-Heuslers with high thermoelectric performance. *Nat. Commun.* **10**, 270 (2019).
11. A. Zevalkink, D. M. Smiadak, J. L. Blackburn, A. J. Ferguson, M. L. Chabiny, O. Delaire, J. Wang, K. Kovnir, J. Martin, L. T. Schelhas, T. D. Sparks, S. D. Kang, M. T. Dylla, G. J. Snyder, B. R. Ortiz, E. S. Toberer, A practical field guide to thermoelectrics: Fundamentals, synthesis, and characterization. *Appl. Phys. Rev.* **5**, 021303 (2018).
12. E. S. Toberer, M. Christensen, B. B. Iversen, G. J. Snyder, High temperature thermoelectric efficiency in $\text{Ba}_8\text{Ga}_{16}\text{Ge}_{30}$. *Phys. Rev. B* **77**, 075203 (2008).
13. K. Akai, T. Uemura, K. Kishimoto, T. Tanaka, H. Kurisu, S. Yamamoto, T. Koyanagi, K. Koga, H. Anno, M. Matsuura, First-principles study of semiconducting clathrate $\text{Ba}_8\text{Al}_{16}\text{Ge}_{30}$. *J. Electron. Mater.* **38**, 1412–1417 (2009).
14. H. Xie, H. Wang, Y. Pei, C. Fu, X. Liu, G. J. Snyder, X. Zhao, T. Zhu, Beneficial contribution of alloy disorder to electron and phonon transport in half-Heusler thermoelectric materials. *Adv. Funct. Mater.* **23**, 5123–5130 (2013).
15. X. Shi, Y. Pei, G. J. Snyder, L. Chen, Optimized thermoelectric properties of $\text{Mo}_3\text{Sb}_{7-x}\text{Te}_x$ with significant phonon scattering by electrons. *Energ. Environ. Sci.* **4**, 4086–4095 (2011).
16. H.-S. Kim, N. A. Heinz, Z. M. Gibbs, Y. Tang, S. D. Kang, G. J. Snyder, High thermoelectric performance in $(\text{Bi}_{0.25}\text{Sb}_{0.75})_2\text{Te}_3$ due to band convergence and improved by carrier concentration control. *Mater. Today* **20**, 452–459 (2017).
17. I. T. Witting, F. Ricci, T. C. Chasapis, G. Hautier, G. J. Snyder, The thermoelectric properties of *n*-type bismuth telluride: Bismuth selenide alloys $\text{Bi}_2\text{Te}_{3-x}\text{Se}_x$. *Research* **2020**, 4361703 (2020).
18. Y. Pei, X. Shi, A. LaLonde, H. Wang, L. Chen, G. J. Snyder, Convergence of electronic bands for high performance bulk thermoelectrics. *Nature* **473**, 66–69 (2011).
19. A. F. May, D. J. Singh, G. J. Snyder, Influence of band structure on the large thermoelectric performance of lanthanum telluride. *Phys. Rev. B* **79**, 153101 (2009).
20. Y. Tang, Z. M. Gibbs, L. A. Agapito, G. Li, H.-S. Kim, M. B. Nardelli, S. Curtarolo, G. J. Snyder, Convergence of multi-valley bands as the electronic origin of high thermoelectric performance in CoSb_3 skutterudites. *Nat. Mater.* **14**, 1223–1228 (2015).
21. H. Kamila, P. Sahu, A. Sankhla, M. Yasseri, H.-N. Pham, T. Dasgupta, E. Mueller, J. de Boor, Analyzing transport properties of *p*-type $\text{Mg}_3\text{Si}-\text{Mg}_3\text{Sn}$ solid solutions: Optimization of thermoelectric performance and insight into the electronic band structure. *J. Mater. Chem. A* **7**, 1045–1054 (2019).
22. Y. Pei, H. Wang, G. J. Snyder, Band engineering of thermoelectric materials. *Adv. Mater.* **24**, 6125–6135 (2012).
23. E. S. Toberer, C. A. Cox, S. R. Brown, T. Ikeda, A. F. May, S. M. Kauzlarich, G. J. Snyder, Traversing the metal-insulator transition in a Zintl phase: Rational enhancement of thermoelectric efficiency in $\text{Yb}_{14}\text{Mn}_{1-x}\text{Al}_x\text{Sb}_{11}$. *Adv. Funct. Mater.* **18**, 2795–2800 (2008).
24. A. F. May, G. J. Snyder, Introduction to modeling thermoelectric transport at high temperatures. *Thermoelect. Energ.*, K1–K18 (2012).
25. E. L. Kunz Wille, N. S. Grewal, S. K. Bux, S. M. Kauzlarich, Seebeck and figure of merit enhancement by rare Earth doping in $\text{Yb}_{14-x}\text{RE}_x\text{ZnSb}_{11}$ ($x = 0.5$). *Materials* **12**, 731–743 (2019).
26. Y. Hu, J. Wang, A. Kawamura, K. Kovnir, S. M. Kauzlarich, $\text{Yb}_{14}\text{MgSb}_{11}$ and $\text{Ca}_{14}\text{MgSb}_{11}$ —New Mg-containing Zintl compounds and their structures, bonding, and thermoelectric properties. *Chem. Mater.* **27**, 343–351 (2014).
27. W. Tan, Z. Wu, M. Zhu, J. Shen, T. Zhu, X. Zhao, B. Huang, X.-t. Tao, S.-q. Xia, $\text{A}_1\text{MgBi}_{11}$ ($\text{A} = \text{Ca}, \text{Sr}, \text{Eu}$): Magnesium bismuth based Zintl phases as potential thermoelectric materials. *Inorg. Chem.* **56**, 10576–10583 (2017).
28. Y. Wang, Y.-J. Hu, S. A. Firdosy, K. E. Star, J.-P. Fleurial, V. A. Ravi, L.-Q. Chen, S.-L. Shang, Z.-K. Liu, First-principles calculations of lattice dynamics and thermodynamic properties for $\text{Yb}_{14}\text{MnSb}_{11}$. *J. Appl. Phys.* **123**, 045102 (2018).
29. M. T. Agne, R. Hanus, G. J. Snyder, Minimum thermal conductivity in the context of diffusion-mediated thermal transport. *Energ. Environ. Sci.* **11**, 609–616 (2018).
30. C. J. Perez, X. Qi, Z. Chen, S. K. Bux, S. Chanakain, B. Li, K. Liu, R. Dhall, K. C. Bustillo, S. M. Kauzlarich, Improved power factor and mechanical properties of composites of $\text{Yb}_{14}\text{MgSb}_{11}$ with iron. *ACS Appl. Energy Mater.* **3**, 2147–2159 (2020).
31. S. J. Gomez, D. Cheikh, T. Vo, P. Von Allmen, K. Lee, M. Wood, G. J. Snyder, B. S. Dunn, J.-P. Fleurial, S. K. Bux, Synthesis and characterization of vacancy-doped neodymium telluride for thermoelectric applications. *Chem. Mater.* **31**, 4460–4468 (2019).
32. S. Sarkar, X. Zhang, S. Hao, X. Hua, T. P. Bailey, C. Uher, C. Wolverton, V. P. Dravid, M. G. Kanatzidis, Dual alloying strategy to achieve a high thermoelectric figure of merit and lattice hardening in *p*-Type nanostructured PbTe . *ACS Energy Lett.* **3**, 2593–2601 (2018).
33. W. Li, S. Lin, M. Weiss, Z. Chen, J. Li, Y. Xu, W. G. Zeier, Y. Pei, Crystal structure induced ultralow lattice thermal conductivity in thermoelectric Ag_9AlSe_6 . *Adv. Energy Mater.* **8**, 1800030 (2018).

34. N. Kazem, J. V. Zaikina, S. Ohno, G. J. Snyder, S. M. Kauzlarich, Coinage-metal-stuffed $\text{Eu}_9\text{Cd}_4\text{Sb}_5$: Metallic compounds with anomalous low thermal conductivities. *Chem. Mater.* **27**, 7508–7519 (2015).

35. E. L. Kunz Wille, N. H. Jo, J. C. Fettinger, P. C. Canfield, S. M. Kauzlarich, Single crystal growth and magnetic properties of the mixed valent Yb containing Zintl phase, $\text{Yb}_{14}\text{MgSb}_{11}$. *Chem. Commun.* **54**, 12946–12949 (2018).

36. A. He, E. L. Kunz Wille, L. M. Moreau, S. M. Thomas, J. M. Lawrence, E. D. Bauer, C. H. Booth, S. M. Kauzlarich, Intermediate Yb Valence in the Zintl phases $\text{Yb}_{14}\text{MSb}_{11}$ ($\text{M} = \text{Zn, Mn, Mg}$): XANES, magnetism, and heat capacity. *Phys. Rev. Mater.* **4**, 114407 (2020).

37. A. P. Holm, T. C. Ozawa, S. M. Kauzlarich, S. A. Morton, G. Dan Waddill, J. G. Tobin, X-ray photoelectron spectroscopy studies of $\text{Yb}_{14}\text{MnSb}_{11}$ and $\text{Yb}_{14}\text{ZnSb}_{11}$. *J. Solid State Chem.* **178**, 262–269 (2005).

38. H. J. Goldsmid, J. W. Sharp, Estimation of the thermal band gap of a semiconductor from Seebeck measurements. *J. Electron. Mater.* **28**, 869–872 (1999).

39. R. W. McKinney, P. Gorai, V. Stevanović, E. S. Toberer, Search for new thermoelectric materials with low Lorenz number. *J. Mater. Chem. A* **5**, 17302–17311 (2017).

40. A. Putatunda, D. J. Singh, Lorenz number in relation to estimates based on the Seebeck coefficient. *Mater. Today Phys.* **8**, 49–55 (2019).

41. M. Thesberg, H. Kosina, N. Neophytou, On the Lorenz number of multiband materials. *Phys. Rev. B* **95**, 125206 (2017).

42. Y. Pei, A. D. LaLonde, H. Wang, G. J. Snyder, Low effective mass leading to high thermoelectric performance. *Energ. Environ. Sci.* **5**, 7963–7969 (2012).

43. H. Wang, Y. Pei, A. D. LaLonde, G. J. Snyder, Material Design Considerations Based on Thermoelectric Quality Factor, in *Thermoelectric Nanomaterials: Materials Design and Applications*, K. Koumoto, T. Mori, Eds. (Springer Berlin Heidelberg, Berlin, Heidelberg, 2013), pp. 3–32.

44. Y. Hu, K. Lee, S. M. Kauzlarich, Optimization of $\text{Ca}_{14}\text{MgSb}_{11}$ through chemical substitutions on Sb sites: Optimizing Seebeck coefficient and resistivity simultaneously. *Crystals* **8**, 211–221 (2018).

45. J. F. Rauscher, C. A. Cox, T. Yi, C. M. Beavers, P. Klavins, E. S. Toberer, G. J. Snyder, S. M. Kauzlarich, Synthesis, structure, magnetism, and high temperature thermoelectric properties of Ge doped $\text{Yb}_{14}\text{MnSb}_{11}$. *Dalton Trans.* **39**, 1055–1062 (2010).

46. S. R. Brown, E. S. Toberer, T. Ikeda, C. A. Cox, F. Gascoin, S. M. Kauzlarich, G. J. Snyder, Improved thermoelectric performance in $\text{Yb}_{14}\text{Mn}_{1-x}\text{Zn}_x\text{Sb}_{11}$ by the reduction of spin-disorder scattering. *Chem. Mater.* **20**, 3412–3419 (2008).

47. V. Petříček, M. Dušek, L. Palatinus, in *Zeitschrift für Kristallographie - Crystalline Materials* (De Gruyter, 2014), vol. 229, pp. 345.

48. T. Hom, W. Kiszenik, B. Post, Accurate lattice constants from multiple reflection measurements. II. Lattice constants of germanium silicon, and diamond. *J. Appl. Cryst.* **8**, 457–458 (1975).

49. J.-F. Bérar, P. Lelann, E.s.d.'s and estimated probable error obtained in Rietveld refinements with local correlations. *J. Appl. Cryst.* **24**, 1–5 (1991).

50. V. Ravi, S. Firdosy, T. Caillat, E. Brandon, K. Van Der Walde, L. Maricic, A. Sayir, Thermal expansion studies of selected high-temperature thermoelectric materials. *J. Electron. Mater.* **38**, 1433–1442 (2009).

51. C. A. Cox, E. S. Toberer, A. A. Levchenko, S. R. Brown, G. J. Snyder, A. Navrotsky, S. M. Kauzlarich, Structure, heat capacity, and high-temperature thermal properties of $\text{Yb}_{14}\text{Mn}_{1-x}\text{Al}_x\text{Sb}_{11}$. *Chem. Mater.* **21**, 1354–1360 (2009).

52. K. A. Borup, E. S. Toberer, L. D. Zoltan, G. Nakatsukasa, M. Errico, J.-P. Fleurial, B. B. Iversen, G. J. Snyder, Measurement of the electrical resistivity and Hall coefficient at high temperatures. *Rev. Sci. Instrum.* **83**, 123902 (2012).

53. C. Wood, D. Zoltan, G. Stauffer, Measurement of Seebeck coefficient using a light-pulse. *Rev. Sci. Instrum.* **56**, 719–722 (1985).

54. W. Kohn, L. J. Sham, Self-consistent equations including exchange and correlation effects. *Phys. Rev.* **140**, A1133–A1138 (1965).

55. P. E. Blöchl, Projector augmented-wave method. *Phys. Rev. B Condens. Matter* **50**, 17953 (1994).

56. G. Kresse, D. Joubert, From ultrasoft pseudopotentials to the projector augmented-wave method. *Phys. Rev. B* **59**, 1758–1775 (1999).

57. J. P. Perdew, K. Burke, M. Ernzerhof, Generalized gradient approximation made simple. *Phys. Rev. Lett.* **77**, 3865–3868 (1996).

58. J. A. Cooley, P. Promkhan, S. Gangopadhyay, D. Donadio, W. E. Pickett, B. R. Ortiz, E. S. Toberer, S. M. Kauzlarich, High seebeck coefficient and unusually low thermal conductivity near ambient temperatures in layered compound $\text{Yb}_2-x\text{Eu}_x\text{CdSb}_2$. *Chem. Mater.* **30**, 484–493 (2017).

59. G. K. H. Madsen, D. J. Singh, BoltzTraP. A code for calculating band-structure dependent quantities. *Comput. Phys. Commun.* **175**, 67–71 (2006).

60. G. K. H. Madsen, J. Carrete, M. J. Verstraete, BoltzTraP2, a program for interpolating band structures and calculating semi-classical transport coefficients. *Comput. Phys. Commun.* **231**, 140–145 (2018).

61. S. P. Ong, W. D. Richards, A. Jain, G. Hautier, M. Kocher, S. Cholia, D. Gunter, V. L. Chevrier, K. A. Persson, G. Ceder, Python Materials Genomics (pymatgen): A robust, open-source python library for materials analysis. *Comput. Mater. Sci.* **68**, 314–319 (2013).

62. A. Jain, S. P. Ong, G. Hautier, W. Chen, W. D. Richards, S. Dacek, S. Cholia, D. Gunter, D. Skinner, G. Ceder, K. A. Persson, Commentary: The Materials Project: A materials genome approach to accelerating materials innovation. *APL Mater.* **1**, 011002 (2013).

63. W. Setyawan, S. Curtarolo, High-throughput electronic band structure calculations: Challenges and tools. *Comput. Mater. Sci.* **49**, 299–312 (2010).

64. S. D. Kang, G. J. Snyder, Charge-transport model for conducting polymers. *Nat. Mater.* **16**, 252–257 (2017).

65. B. M. Askerov, *Electron Transport Phenomena in Semiconductors* (World Scientific, 1994).

66. V. I. Fistul, *Heavily Doped Semiconductors* (Springer Science & Business Media, 2012), vol. 1.

67. J. M. Ziman, *Electrons and Phonons: The Theory of Transport Phenomena in Solids* (Oxford Univ. Press, 2001).

68. G. J. Snyder, A. H. Snyder, M. Wood, R. Gurunathan, B. H. Snyder, C. Niu, Weighted mobility. *Adv. Mater.* **32**, e2001537 (2020).

Acknowledgments: We thank N. Botto for assistance with EMPA measurements and G. Gerig for Seebeck measurements. **Funding:** This work was supported by the NSF (DMR-1709382 and DMR-2001156-0) and the NASA Science Missions Directorate's Radioisotope Power Systems Program. Part of this work was conducted at the Jet Propulsion Laboratory California Institute of Technology under contract with the National Aeronautics and Space Administration with funding from the Science Mission Directorate's Radioisotope Power Systems program. G.Y. and F.R. acknowledge financial support from the F.R.S.-FNRS project HTBaSE (contract no. PDR-T.1071.15) and the Low Cost ThermoElectric Devices (LOCOTED) project funded by the Région Wallonne (Programmes FEDER). Computational resources have been provided by the supercomputing facilities of the Consortium des Équipements de Calcul Intensif en Fédération Wallonie-Bruxelles de (CECI) funded by the F.R.S.-FNRS, and the Tier-1 supercomputer of the Fédération Wallonie-Bruxelles, infrastructure funded by the Walloon Region under the grant agreement number 1117545. **Author contributions:** The paper was written collaboratively by C.J.P., M.W., and S.M.K. and with input from all other authors. Synthesis, structural characterization, and thermoelectric property measurements were performed by C.J.P. M.W. developed the multiband model. G.H., G.-M.R., G.Y., and F.R. performed the electronic structure calculations with initial calculations performed by T.V. S.M.K., S.K.B., C.J.P., and M.W. designed the project. **Competing interests:** The authors declare that they have no competing interests. **Data and materials availability:** All data needed to evaluate the conclusions in the paper are present in the paper and/or the Supplementary Materials. Additional data related to this paper may be requested from the authors.

Submitted 24 September 2020

Accepted 1 December 2020

Published 20 January 2021

10.1126/sciadv.abe9439

Citation: C. J. Perez, M. Wood, F. Ricci, G. Yu, T. Vo, S. K. Bux, G. Hautier, G.-M. Rignanese, G. J. Snyder, S. M. Kauzlarich, Discovery of multivalley Fermi surface responsible for the high thermoelectric performance in $\text{Yb}_{14}\text{MnSb}_{11}$ and $\text{Yb}_{14}\text{MgSb}_{11}$. *Sci. Adv.* **7**, eabe9439 (2021).

Science Advances

Discovery of multivalley Fermi surface responsible for the high thermoelectric performance in Yb₁₄MnSb₁₁ and Yb₁₄MgSb₁₁

Christopher J. Perez, Maxwell Wood, Francesco Ricci, Guodong Yu, Trinh Vo, Sabah K. Bux, Geoffroy Hautier, Gian-Marco Rignanese, G. Jeffrey Snyder and Susan M. Kauzlarich

Sci Adv 7 (4), eabe9439.
DOI: 10.1126/sciadv.abe9439

ARTICLE TOOLS

<http://advances.sciencemag.org/content/7/4/eabe9439>

SUPPLEMENTARY MATERIALS

<http://advances.sciencemag.org/content/suppl/2021/01/14/7.4.eabe9439.DC1>

REFERENCES

This article cites 60 articles, 0 of which you can access for free
<http://advances.sciencemag.org/content/7/4/eabe9439#BIBL>

PERMISSIONS

<http://www.sciencemag.org/help/reprints-and-permissions>

Use of this article is subject to the [Terms of Service](#)

Science Advances (ISSN 2375-2548) is published by the American Association for the Advancement of Science, 1200 New York Avenue NW, Washington, DC 20005. The title *Science Advances* is a registered trademark of AAAS.

Copyright © 2021 The Authors, some rights reserved; exclusive licensee American Association for the Advancement of Science. No claim to original U.S. Government Works. Distributed under a Creative Commons Attribution NonCommercial License 4.0 (CC BY-NC).